Raman spectroscopy: Nanostructures

Xin Zhang and Ping-Heng Tan, State Key Laboratory of Superlattices and Microstructures, Institute of Semiconductors, Chinese Academy of Sciences, Beijing, China

© 2024 Elsevier Ltd. All rights reserved.

Abstract

Raman spectroscopy provides information on the structure, electronic and vibrational properties of crystals by the inelastic photon scattering effect. It has been a fast and nondestructive characterization tool with high spatial and spectral resolutions, which is preferential to nanostructures. The classical and quantum theory of Raman scattering effect is introduced, with the emphasis on the basic features of a Raman spectrum. Phonons in nanostructures are first exampled by the case of a semiconductor superlattice and then extended into other systems based on their Raman spectra. The applications of resonance Raman scattering are demonstrated by studying the phonon dispersion, electronic structure and enhancement of interlayer shear phonon in carbon materials.

Key points

- Classical and quantum ways to understand Raman scattering effect
- Key parameters of a Raman spectrum
- Size impacts on Raman scattering in nanostructures
- Various types of phonons subject to nanostructures
- Resonant Raman scattering effects

Introduction

Light interacts with matter in many different ways (Fox, 2010). The photons which make up the light may be absorbed or scattered or directly pass through without any interactions with the medium. Scattering specifies the phenomenon in which the light changes direction and is said to be inelastic (elastic) if the frequency of the scattered light is changed (unchanged). The phenomenon of inelastic light scattering was first postulated by Smekal (1923) and first observed experimentally in 1928 by Raman and Krishnan in molecules (Raman and Krishnan, 1928) referred to as Raman scattering since then. Over nearly one century, Raman scattering effect has been widely used to provide information on chemical structures and physical properties of materials (Jorio et al., 2011; Tan, 2019; Toporski et al., 2018), through its spectroscopy measurements (so-called Raman spectroscopy). To obtain a Raman spectrum requires a specialized apparatus with the capability to resolve a relatively weak Raman signal that is much close in energy to the elastically scattered light. Thanks to the developments of advanced apparatus (Demtroder, 2003) like lasers, charge-coupled detectors, optical filters, etc., modern Raman spectroscopy (Smith and Dent, 2019) becomes an essential tool to study the electronic (Schuller, 2006) and vibrational (Stroscio and Dutta, 2001) properties of nanostructures.

Nanostructure features a typical size in the range $1\sim100$ nm in either one (called two-dimensional system, 2D system), two (one-dimensional system, 1D system), three dimensions (zero-dimensional system, 0D system), as exampled by a quantum well, quantum wire and quantum dot (Davies, 1997), respectively. Notably, nanoplate (quasi-2D system), nanowire (quasi-1D system) and nanocrystal (quasi-0D system) are regularly used as the typical size is larger than (but close to) the characteristic length understudied. The reduced size of nanostructure distinguishes its Raman scattering effect from the bulk case (Zhang, 2012), from the aspects of the energy dispersion, momentum conservation and symmetry of vibration modes. As the quantized electrons are

confined in a square/parabolic quantum well, there are similar quantized phonons that are confined within a phonon quantum well, as illustrated in Fig. 2(b). In addition, as the surface-to-volume is significantly increased in nanostructures, various types of surface/interface-associated phonons appear. The constraints by momentum conservation in Raman scattering process are degraded as the momentum uncertainty ($\Delta q \leq \hbar/\Delta r$) inevitably increases due to the reduced size in nanostructures. It will include those phonons with momentum lying within Δq to participate in the Raman scattering events. The symmetry of vibration mode, which determines if the mode is Raman active or not, is reduced as the dimensionality of nanostructures decreases. It may allow the observation of those forbidden modes in bulk cases. On the other hand, the quantized electrons feature a large density of states, which is readily exploited to enhance those weak Raman signals in both nanostructures and bulk structures. It is enabled by the resonance electronic transition (Cardona, 1975; Jorio et al., 2011), so-called resonance Raman scattering (RRS), which greatly enhances the electronic transition and electron-phonon scattering rates.

Overview

The section "Raman Spectroscopy basics" provides the fundamental theory for Raman scattering effect in both classical and quantum ways from which the general features of a specific Raman spectrum are summarized. The various types of vibration modes are introduced in the section "Phonons in nanostructures" which covers the confined, interface, surface and folded vibration modes, first introduced by an exampled superlattice (SL) and then expanded into other typical nanostructures. The third section is given to "Resonance Raman scattering in nanostructures" which specifies the contributions of resonance electronic transition to the Raman intensity enhancements and the applications to study the phonon dispersion, electronic structure and enhancement of interlayer shear phonon in carbon-related materials.

Raman spectroscopy basics

Raman scattering effect can be understood simply by the classical electromagnetic theory (Cardona, 1975; Jorio et al., 2011). An incident electric field E when applied to a solid will induce a polarization P resulting $P = \varepsilon_0 \chi E$, with ε_0 and χ the permittivity and the electronic susceptibility of the medium, respectively. χ is to measure the ability of the incident electric field to shake the electrons of atoms in the solid, as illustrated in Fig. 1(a), which is naturally modulated by the lattice vibration with a frequency ω_q in the solid,

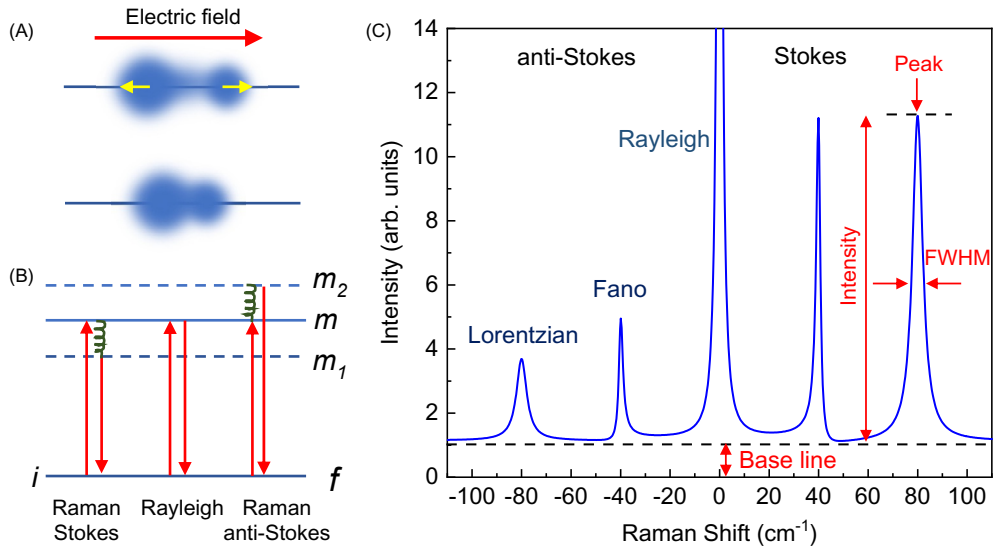

Fig. 1 (a) Schematics show how the lattice vibration changes the electronic susceptibility χ of the diatomic linear chain. When the two atoms get closer and far away along the chain direction, it will be respectively harder and easier for the electric field to shape the electron clouds. (b) Schematics show the third-order process to describe the Raman scattering process in crystals. The horizontal line is the electronic energy level and the solid (dashed) line is the real (virtual) state. The large upwards $i \rightarrow m$ and downwards m (including m_1 and m_2) $\rightarrow f$ arrows represent photon absorption and emission by electrons, while the small downwards ($m \rightarrow m_1$) and upwards ($m \rightarrow m_2$) arrows represent respectively the electron losing (obtaining) energy to (from) the lattice by an electron-phonon scattering event, accordingly known as Raman Stokes (anti-Stokes) process. Rayleigh scattering refers to the case without any energy changes of the electron in m state. (c) One artificial Raman spectrum to show the spectral features and the typical parameters. Rayleigh (at 0 cm^{-1}) intensity is always much stronger and it has to be filtered out for any Raman measurements. The Stokes processes (>0 cm^{-1}) are normally stronger than the anti-Stokes processes (<0 cm^{-1}) due to phonon creation/annihilation statistics. Raman peaks have a Lorentz lineshape featured by Peak, Intensity and the full width at half maximum (FWHM). In specific cases, the Raman features exhibit a Breit-Wigner-Fano (BWF) lineshape. Notably, the real Raman spectrum contains a baseline determined by the noise performance of the measurement system.

to the first-order, $\chi = \chi_0 + \left(\frac{\partial \chi}{\partial Q}\right)_0 Q(\omega_q)$, with $Q(\omega_q) = Q \sin \omega_q t$ the atomic displacements. In light scattering experiments, E is oscillating at an optical frequency ω_i, $E = E_0 \sin \omega_i t$. The polarization induced by electric field now becomes

$$P = \varepsilon_0 \chi_0 E_0 \sin \omega_i t + \frac{A}{2}\left[\cos\left(\omega_i - \omega_q\right)t - \cos\left(\omega_i + \omega_q\right)t\right] \tag{1}$$

with $A = \varepsilon_0 \left(\frac{\partial \chi}{\partial Q}\right)_0 Q E_0$. Eq. (1) points out that light will be scattered both elastically at a frequency ω_i (Rayleigh scattering) and inelastically, being downshifted (emission of a phonon) by the vibration frequency ω_q in the solid (Raman Stokes process) or upshifted (absorption of a phonon) by the same frequency ω_q (Raman anti-Stokes process). The differential Raman scattering cross section is obtained by (Cardona, 1975)

$$\frac{d\sigma}{d\Omega} = \frac{\omega_s^4}{(4\pi)^2 c^4}\left|\widehat{e}_L \cdot \left(\frac{\partial \chi}{\partial Q}\right)_0 Q(\omega_q) \cdot \widehat{e}_S\right|^2 \tag{2}$$

where the optical frequency of scattered light $\omega_s = \omega_i \pm \omega_q$ as indicated in Eq. (1), c the speed of light in the medium, $\widehat{e}_L$ ($\widehat{e}_S$) the unit vector representing the polarization of the incident (scattered) light. The Raman tensor can be further defined from Eq. (2), as $R = \left(\frac{\partial \chi}{\partial Q}\right)_0 \widehat{Q}(\omega_q)$, with $\widehat{Q} = Q/|Q|$ the unit vector, which is a third-order tensor. The full list of Raman tensors to seven types of crystal systems can be found in textbooks (Jorio et al., 2011; Zhang, 2012). Raman tensor is key to probe the symmetry of lattice vibration, implemented in polarized Raman spectroscopy measurements.

A quantum mechanical description of Raman scattering effect is based on the so-called Fermi's Golden Rule, which is used to calculate the transition probability per unit time when considering the optical properties of solids (Fox, 2010; Jorio et al., 2011). W_{if} describes a transition from an initial state $|i\rangle$ to a final one $|f\rangle$, which results

$$W_{if} \cong \frac{2\pi}{\hbar}|\langle f|H'|i\rangle|^2 \rho(E_f)\delta(E_f - E_i) \tag{3}$$

with H' the Hamiltonian to account for the interaction between the electromagnetic radiation and the crystal, $\rho(E_f)$ density of final states assuming the discrete initial state. In the first-order Raman scattering process, as shown in Fig. 1(b), H' includes three types of interactions, which can be interpreted as three steps: (1) the incident light excites the electron from an initial state $|i\rangle$ with energy E_i, to a higher energy state $|m\rangle$ with energy E_m from a laser (E_L). The solid line of state $|m\rangle$ represents a real electronic state, allowing a resonant light absorption process. (2) The electron is further scattered by a phonon to a "virtual" state (dashed line) $|m_1\rangle$ (Stokes) or $|m_2\rangle$ (anti-Stokes). Noted virtual states are usually displayed by dashed lines and, within perturbation theory, they are described by a linear combination of the electron eigenstates of the system with a large energy uncertainty and a small lifetime to compensate for the uncertainty principle. (3) The scattered electron finally decays back to the state $|i\rangle$ by emitting the scattered light. Noted the whole system is now labeled as the state $|f\rangle$ since additional phonon is emitted or absorbed with respect to the initial state $|i\rangle$. The differential Raman scattering cross section is accordingly obtained by third-order perturbation theory (Jorio et al., 2011) which gives

$$\frac{d\sigma}{d\Omega} \propto |\langle f|H'|i\rangle|^2 = \left|\sum_{m,m'} \frac{M^{op}(k_i - q, im')M^{ep}(q, m'm)M^{op}(k_i, mi)}{(E_L - \Delta E_{mi})(E_L - \hbar\omega_q - \Delta E_{m'i})}\right|^2 \tag{4}$$

in which $\Delta E_{m'i} = (E_{m'} - E_i) - i\gamma$, where m and m' denote the two excited intermediate states, γ denotes the broadening factor of the resonance event, M^{op} and M^{ep} respectively denote the electric dipole matrix elements of the electron-photon and the electron-phonon interactions. A high-order Raman process, having the various transition diagrams (Yu and Cardona, 2010), can be described by high-order perturbation theory. The denominator in Eq. (4) determines the resonance condition in RRS, which is classified as an incident resonance when $E_L = E_m - E_i$, or a scattered resonance when $E_L - \hbar\omega_q = E_{m'} - E_i$. The resonance effect is essential to the observations of measurable Raman signals from nano-scale systems. A plot of Eq. (4) as a function of E_L gives the Raman excitation profile which is essential to provide the information about the electronic structure of nanostructures (Cardona, 1975).

A Raman spectrum is a plot of the intensity of the scattered light as a function of Raman shift, $\omega = \omega_i - \omega_s$, which is $\pm\omega_q$ according to Eq. (1). Thus, the spectrum exhibits a pair of peaks on the sides of the Rayleigh line, as shown in Fig. 1(c), but either one (usually the Stokes one) or both are recorded depending on the Raman filters available in the practice Raman spectrum measurements. The phonon excitation can be considered as a harmonic oscillator damped by the interaction with other excitations in the medium. Therefore, the Raman spectrum usually features a forced damped harmonic oscillator with a Lorentzian curve given by

$$I(\omega) = \frac{I_0}{\pi\Gamma_q}\frac{1}{(\omega - \omega_q)^2 + \Gamma_q^2} \tag{5}$$

in the limit where the frequency $\omega_q \gg \Gamma_q$, with Γ_q the inverse of the lifetime for a phonon, usually expressed by the full width at half maximum intensity (FWHM), FWHM $= 2\Gamma_q$. In specific cases, such as lattice vibration couples to an electronic continuum, the Raman lineshape can deviate from the simple Lorentzian curve and exhibit a so-called Breit-Wigner-Fano (BWF) lineshape, which is given by

$$I(\omega) = I_0\frac{[1 + (\omega - \omega_0)/q\Gamma]^2}{1 + [(\omega - \omega_0)/\Gamma]^2} \tag{6}$$

where $1/q$ is a measure of the interaction of a discrete level (phonon) with a continuum of states (the electrons). ω_0 is the BWF peak frequency at maximum intensity I_0, and Γ is the half width of the BWF peak. A pair of BWF peaks with $1/q > 0$ is plotted in Fig. 1(c). Such effect is observed in the ultralow-frequency Raman spectra of a multilayer graphene (Tan et al., 2012), as shown in Fig. 6(d). From Eq. (2), the differential Raman scattering cross section for Stokes and anti-Stokes are obtained by (Cardona, 1975)

$$\begin{aligned}\frac{d\sigma_S}{d\Omega} &\propto \langle Q(\omega_q)Q^*(\omega_q)\rangle \propto (n+1)\\ \frac{d\sigma_{aS}}{d\Omega} &\propto \langle Q^*(\omega_q)Q(\omega_q)\rangle \propto n\end{aligned} \tag{7}$$

where $n = (\exp(\hbar\omega_q/k_BT) - 1)^{-1}$ is Bose-Einstein distribution function for the phonon with energy $\hbar\omega_q$. So the intensity of Raman Stokes process is much stronger than the anti-Stokes case by noticing

$$\frac{\sigma_S}{\sigma_{aS}} \propto \exp\left(\frac{\hbar\omega_q}{k_BT}\right) \gg 1 \tag{8}$$

Finally, energy and momentum conservations can respectively be found from Eq. (3), expressed by $\delta(E_f - E_i)$, and Eq. (4), by $k_s = k_i - q$, i.e., $q \sim 0$ because k_i is much small compared to the dimensions of Brillouin zone (BZ). It is why the first-order Raman process can only probe phonons near the BZ center (Γ point). The Raman frequency of this type of vibration is not dependent on E_L, which was normally taken as the general rule for Raman spectroscopy.

In practice, an efficient collecting system is always required to pick up the relatively weak Raman signals from the strong Rayleigh line. We recommend the book "Modern Raman Spectroscopy: A Practical Approach," written by Ewen Smith and Geoffrey Dent (Smith and Dent, 2019), which can serve as an excellent introduction to the Raman measurement system and the most advanced developments. As complementary, our original work to probe the ultra-low frequency Raman spectra of multilayer graphenes can be referred to as a standard tutorial to introduce the latest advancements to detect those Raman peaks extremely closed to Rayleigh line (Tan et al., 2012).

Phonons in nanostructures

Different types of phonons in nanostructures can be exampled by an SL, as illustrated in Fig. 2(a), which are categorized as the confined optical modes in barrier and well, the macroscopic and microscopic interface modes, and the folded acoustic mode (Tan et al., 2004; Zhang, 2012). The new 1D out-of-plane periods of SL along the growth direction shrink the BZ by folding both the optical and acoustic phonons into a smaller BZ with respect to the bulk case, as shown by Fig. 5(a). Because of the distinctive optical and acoustic vibrations, the folded optical phonons are mostly confined in the alternating layers (confined optical modes), in contrast, the folded acoustic phonons are extended into all of the constitutes of an SL (Fig. 5(a)). As a typical complementary to semiconductor SLs developed in the 1980s, a twisted bilayer system from a 2D material (2DM) holds in-plane artificial periods which create an interesting folding effect on its phonon dispersion (Fig. 5(e)). The confined acoustic and optical modes appear in the case of a strongly confined nanostructure, like nanowire, nanorod and nanocrystal which are normally known as surface vibration modes (Fig. 4). Interface vibration mode is unique in an SL with the macroscopic one from the excited states of the confined optical modes and the microscopic one localized at the interface (which is also known as surface vibration mode). The macroscopic interface modes find their general dispersive behaviors on the layer thickness in multilayer 2DMs (Fig. 3(b)) and distinctive decouples between in-plane and out-of-plane phonons in a 2D van der Waals heterostructures (vdWHs) (Fig. 3(c)). In addition, interface modes apply to the sample-substrate structure (Fig. 3(d)) and the hybrid nanostructures, as exampled by dot-in-rods in Fig. 4(d).

Confined vibration modes

Analogs to the quantization of electrons in a potential well, the frequency of lattice vibration in a "phonon potential well" is well quantized and strongly depends on the length of the potential well. Fig. 2(b) shows the calculated z component of displacements (U_z) for the highest GaAs-like LO modes, LO_1, LO_2, LO_3, in a $(GaAs)_{20}/(AlAs)_{20}$ SL, which are strictly confined in the GaAs layer (Rücker et al., 1992). The profile formed by the displacements of either Ga or As atoms is the same as the quantized electronic wavefunction in a square potential well with the nodes increasing in a sequence of 0,1,2,3, ... (Fig. 2(b)). The confined optical modes within the well layers of quantum well structures were firstly observed in $GaAs/Ga_{1-x}Al_xAs$ SLs (Jusserand et al., 1984). The frequencies of Raman peaks associated with confined phonons show blueshift as decreasing the thickness of GaAs layer, indicated by the pitch arcs labeled by 1, 2, 3, 4 which corresponds to the different confined orders, as shown in Fig. 2(b). The spatial confinement effects on the vibrations in nanostructures are further studied in GaAs/AlAs quantum wire (Comas et al., 1993), silicon nanowire (Piscanec et al., 2003), carbon nanotube (Dresselhaus et al., 2005; Jorio and Saito, 2021), Ge nanocrystal (Bottani et al., 1996), etc. Special attention is paid to the case of nanostructures with intrinsic polarization, such as SiC nanorods (Feng et al., 1988), where the long-range Coulomb interaction results in a Raman spectrum featuring a non-crystallize structure.

Carbon nanotube with a hollow core is different from the semiconductor nanowire but clearly shows the confinement effects. The carbon-related materials involve an optical phonon between the two dissimilar carbon atoms in the unit cell, featuring one single

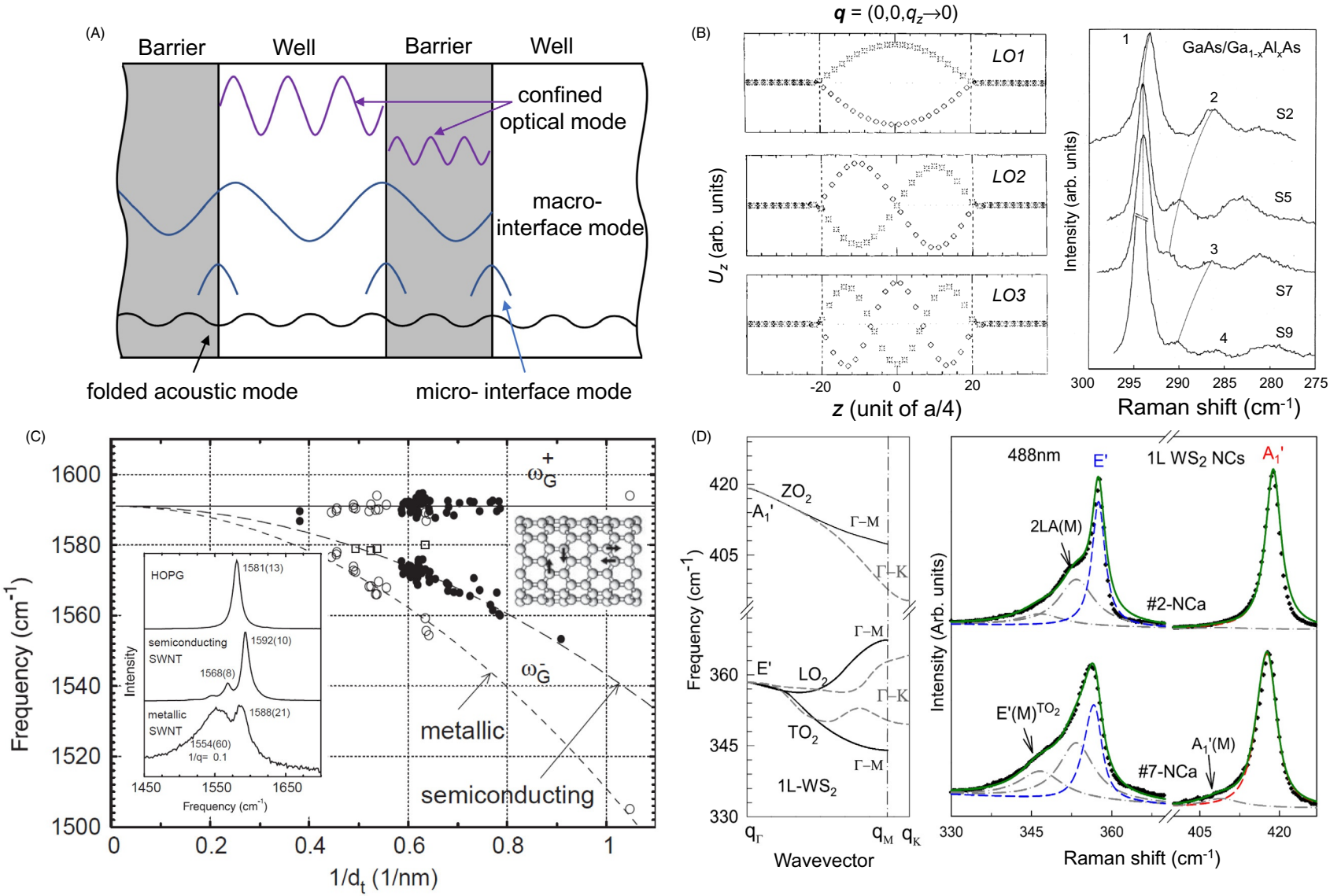

Fig. 2 (a) Five types of vibration modes in a semiconductor superlattice (SL), including the confined optical modes in both barrier and well, the macroscopic (macro-) and microscopic (micro-) interface modes, and the folded acoustic mode. (b) Left: atomic displacements (U_z) of the topmost GaAs-like modes of a (001)-oriented $(GaAs)_{20}/(AlAs)_{20}$ SL for $q = (0, 0, q_z \to 0)$. The GaAs layer is centered at $z = 0$; the dashed vertical lines mark the As interface planes. Diamonds, stars, and asterisks indicate the positions of Ga, Al, and As planes, respectively. Right: Raman spectra of $GaAs/Ga_{1-x}Al_xAs$ SLs in the GaAs optical frequency range. The pitch arcs labeled by 1, 2, 3, 4 correspond to the different confined orders. (c) Frequency as a function of $1/d_t$ for the two most intense G-band features (ω_G^- and ω_G^+) from isolated SWNTs. Insets: Left: the G-band for highly oriented pyrolytic graphite (HOPG), one semiconducting SWNT and one metallic SWNT. Right: atomic vibrations of G-band in SWNT. (d) Left: The phonon branches of 1L-WS_2 related with the E′ and A_1' modes. Right: The experimental (crosses) and fitted (green solid lines) results of two 1L-WS_2 nanocrystals (NCs) with different domain sizes. The blue and red dashed lines are the calculated curves of the E′ and A_1' modes, respectively, and the gray dashed-dotted lines are fittings with Lorentzian peaks to the zone-boundary peaks. The spectra are normalized to A_1' mode. Panel (a): Reproduced from Zhang S.-L. (2012) *Raman Spectroscopy and its Application in Nanostructures*. John Wiley & Sons Ltd. Left Panel (b): Reproduced from Rücker et al. (1992) *Physical Review B* 45: 6747–6756. Right Panel (b): Reproduced from Jusserand et al. (1984) *Physical Review B* 30: 6245–6247. Panel (c): Reproduced from Dresselhaus et al. (2005) *Physics Reports* 409(2): 47–99. Panel (d): Reproduced from Shi et al. (2016) *2D Materials* 3(2): 025016.

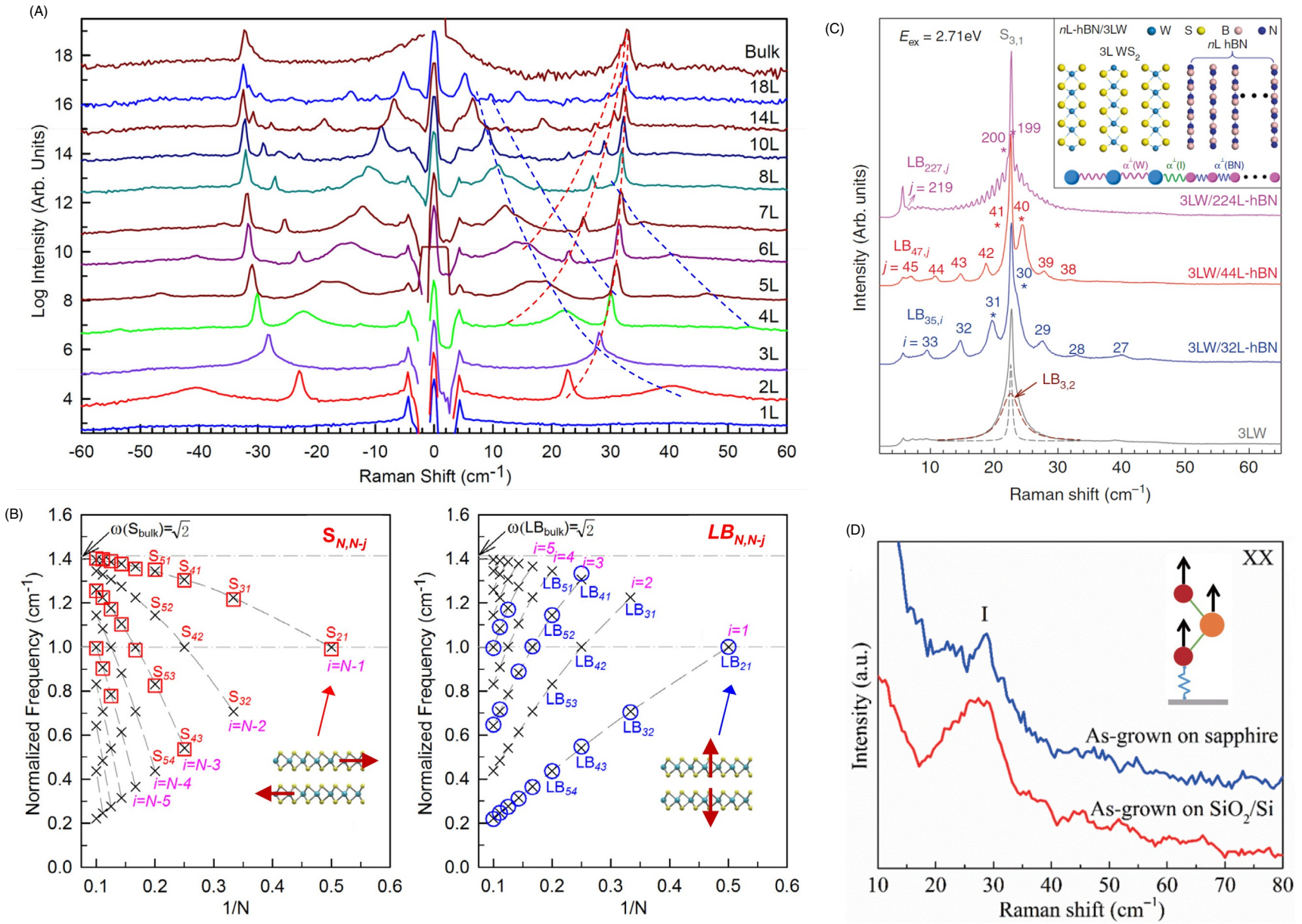

Fig. 3 (a) Stokes and anti-Stokes Raman spectra of *M*- ($N = 1$ -8 , 10, 14 and 18) and bulk MoS_2 between −60 and 60 cm^{-1}. Red and blue dashed lines are guides for the eyes for the frequency trends of the S and LB modes. (b) Fan diagram of the frequencies of interlayer shear (S, Left) and layer-breathing (LB, Right) modes, in a multilayer 2DM as a function of inverse layer number (1/N), with $\omega(S_{2,1})$ and $\omega(LB_{2,1})$ normalized to unity. The subscript $(N, N-j)$ refers to the $(N-j)$th mode of N in a descending sequence. These modes are categorized as branches ($j = N-1, N-2, \ldots$) for the S modes and the branches ($j = 1, 2, \ldots$) for the LB modes. The squares and circles are experimental results from multilayer MoS_2. The atomic insets draw the interlayer S and LB modes in bilayer MoS. Two horizontal dashed lines denote the normalized frequency in bilayer and bulk. (c) Raman spectra of a trilayer WS_2 (3LW) and its heterostructure with a 32 layer, 44 layer and 224 layer hBN, respectively denoted by 3LW/32 L- hBN($\theta_t = 23.5^\circ$), 3LW/ 44L- hBN($\theta_t = 23.5^\circ$) and 3LW/ 224L- hBN($\theta_t = 17.2^\circ$). Inset shows the schematic diagram of a linear chain model for the LB modes in *M*- hBN/3LW. (d) XX-polarized low-frequency Raman spectra of CVD-grown monolayer WS samples on different substrates. Inset: Schematic diagram of the displacement pattern for the interface (I) mode. Panel (a): Reproduced from Zhang et al. (2015) *Chemical Society Reviews* 44: 2757–2785. Panel (b): Reproduced from Zhang et al. (2016) *Nanoscale* 8: 6435–6450. Panel (c): Reproduced from Lin et al. (2019) *Nature Communications* 10(1): 2419. Panel (d): Reproduced from Xiang et al. (2021), *Nano Research* 14(11): 4314–4320.

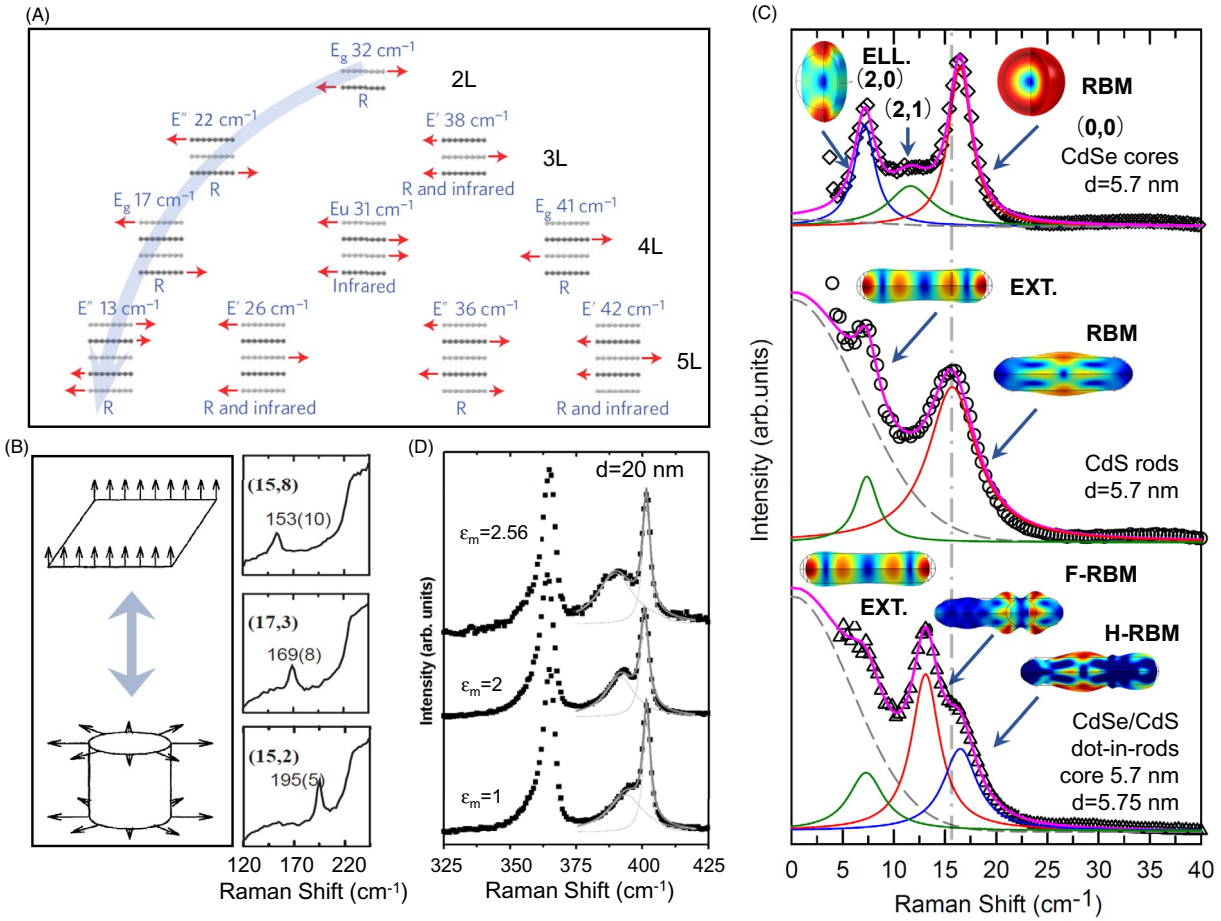

Fig. 4 (a) Symmetry, frequencies and normal mode displacement for each shear mode in multilayer graphene. The Raman-active (R) and infrared-active modes are identified. The arrow denotes the branch of interface vibration modes. (b) Top: The out-of-plane tangential acoustic mode at $k = 0$ (left) in monolayer graphene gives rise to a radial breathing mode (RBM) in the carbon nanotube with non-zero frequency (right). Bottom: RBM Raman spectra for three semiconducting isolated SWNTs of the indicated (n, m) values. (c) Raman spectrum of CdSe nanodot (top), CdS nanorods (middle) and CdSe/CdS dot-in-rods (bottom). Insets show the COMSOL calculations of the deformation. (n, l) is used to assign the ellipsoidal (ELL.) and spheroidal modes of CdSe nanodot. (d) Raman spectra of GaP nanowires with the most probable diameter, $d = 20$ nm, recorded in three different media with different dielectric constants (ε_m). The low, middle and high frequency bands are identified respectively with the TO, SO, and LO phonons. The solid lines represent Lorentzian line shapes used to fit the SO and LO bands. Panel (a): Reproduced from Tan et al. (2012) *Nature Materials* 11(4): 294–300. Top Panel (b): Reproduced from Saito et al. (1998) *Physical Properties of Carbon Nanotubes*. Imperial College Press. Bottom Panel (b): Reproduced from Dresselhaus et al. (2005) *Physics Reports* 409(2): 47–99. Panel (c): Reproduced from Miscuglio et al. (2016) *Nano Letters* 16(12): 7664–7670. Panel (d): Reproduced from Gupta et al. (2003) *Nano Letters* 3(12): 1745–1750.

Lorentzian peak at 1582 cm^{-1} (G-band) for graphite (Dresselhaus et al., 2005; Jorio and Saito, 2021). In contrast, the G-band in a single-wall carbon nanotube (SWNT) consists of two main components, one vibrating along SWNT (LO phonon), locating at ~1590 cm^{-1}(G^+), another one vibrating along the circumferential direction of the SWNT (TO phonon), lying at ~1570 cm^{-1}(G^-), as shown by the inset in Fig. 2(c). Notably, the lineshape of G-peak is highly sensitive to whether the SWNT is metallic (BWF lineshape) or semiconducting (Lorentzian lineshape), as shown by inset in Fig. 2(c). As SWNT curvature increases, i.e., decreasing the SWNT diameter d_t, the frequency of G^- follows a monotonically descending trend both for metallic and semiconducting SWNTs as a result of the stronger spatial confinement. But it does not influence the G^+ peak since it is vibrating along SWNT without any confinements.

The extreme spatial confinements in (quasi-) 0D system, such as quantum dots and nanocrystals (NCs), make the contributions of the confined phonons to its Raman spectrum mixed with the relaxation of the fundamental momentum conservation of $q \sim 0$ required in the Raman scattering process (Sui et al., 1992; Yoshikawa et al., 1995; Zi et al., 1996). It allows those phonons near Γ point in BZ to participate in the scattering process, where the specific phonon dispersion is needed to be included to discuss the lineshape of Raman peaks. In practice, a phonon confinement model (originally proposed by Richter, Wang and Ley, known as RWL model) is widely used (Richter et al., 1981), which gives the Raman intensity in NCs with a domain size L_D as

$$I(\omega) = \int \frac{|C(0,q)|^2}{\left(\omega - \omega_q\right)^2 + \left(\Gamma_0/2\right)^2} d^3q \tag{9}$$

where $|C(0,q)| = \exp(-q^2L_D^2/2\alpha)$ is the Fourier coefficient of a phonon weighting function, with α an adjustable confinement coefficient, Γ_0 is the natural broadening, ω_q is the phonon dispersion curve. The integration is over the BZ. Note, under the circumstance of a Raman peak contributed by a pair of phonon branches which are degenerated at Γ point, as shown in Fig. 2(d) for LO_2 and TO_2, the integration must take them into account. The lineshapes of Raman peaks in NCs are exampled by 2D NCs in monolayer WS_2 (Shi et al., 2016), as shown in Fig. 2(d). The Raman spectra of two 1L-WS_2 NCs in the energy range of the two first-order peaks E' and A_1' are plotted, as well as the good fits including the predictions from Eq. (9). The extracted L_D are 10 nm (#2-NCs) and 2.3 nm (#7-NCs). It indicates a downshift in frequency and an asymmetrical broadening toward lower frequency as L_D decreases. However, an opposite behavior is recovered for A_1' mode in 1L-WSe_2NCs, as a result of its opposite trends of ZO_2 phonon branch away from Γ point in the BZ.

Interface vibration modes

The rapidly developed 2DMs hold a set of unique interface vibrations modes, which are referred to as the interlayer shear (S) and layer-breathing (LB) modes (Zhang et al., 2013, 2015). S and LB modes correspond to the relative motions of the atomic planes which are parallel and perpendicular to the basal plane, respectively. These modes are considered as quasi-acoustic phonons because the atomic vibrations within each layer are in-phase, while the interlayer vibrations are out-of-phase. It indicates that their typical frequencies are relatively small than the optical phonons in 2DMs, as illustrated in Fig. 3(a) for the case of MoS_2. In addition, those modes are highly dispersive as layer number increases. For an N-layer (NL) 2DM, there are (N-1) pairs of S modes and (N-1) pairs of LB modes, which are in sequence denoted as $S_{N,N-j}$ and $LB_{N,\ N-j}$ ($j = 1, 2, \ldots, N-1$) with $S_{N,\ 1}(LB_{N,\ 1})$ the one with the highest frequency. The frequencies of S and LB modes as a function of thickness are well documented by a linear chain mode (LCM) among which each layer of 2DM is simplified as a single ball with an effective mass μ. LCM gives an analytic expression as (Zhang et al., 2016)

$$\begin{aligned}\omega\left(S_{N,N-j}\right) &= \omega(S_{bulk})\sin(j\pi/2N)\\ \omega\left(LB_{N,N-j}\right) &= \omega(LB_{bulk})\sin(j\pi/2N)\end{aligned} \tag{10}$$

where $\omega(S_{bulk}) = \sqrt{\alpha_0^{\parallel}/\pi^2c^2\mu}$ and $\omega(LB_{bulk}) = \sqrt{\alpha_0^{\perp}/\pi^2c^2\mu}$ with c the speed of light, μ the mass per unit area in monolayers, and $\alpha_0^{\parallel}(\alpha_0^{\perp})$ the force constants per unit area for the S (LB) mode. Fig. 3(b) shows the branches ($j = N-1, N-2, \ldots$) for the S modes and the branches ($j = 1, 2, \ldots$) for the LB modes by the scaled $\omega(S_{2,1}) = \omega(LB_{2,1}) = 1$. The normalized experimental frequencies of the S (squares) and LB modes (circles) in NL-MoS_2 by the corresponding $\omega(S_{2,1})$ and $\omega(LB_{2,1})$ perfectly match with the calculations based on LCM. The robust link between $\omega(S_{N,\ N-j})$ (and $\omega(LB_{N,\ N-j})$) and N makes itself an accurate and effective method to identify the thickness of a specific multilayer 2DM.

Interface vibration modes also apply to vdWHs which combine two different 2DMs, but have distinctive features with respect to natural 2DMs. Fig. 3(c) shows the Raman spectra of the vdWHs formed by interfacing a trilayer WS_2 (3LW) with N Layer hBN (NL-hBN, $N = 32$, 44, and 224), as compared with that of a standalone 3LW (Lin et al., 2019). The S mode in vdWHs is localized within 3LW ($S_{3,1}$) consitituent, in contrast, the LB modes are well extended over the entire layers of the vdWHs, exhibiting bulk-like phonon features. It is surprising to observe more than 30 LB modes in 3 LW/224L-hBN vdWHs, which are resonantly enhanced by electronic transitions related to the C exciton of the 3LW. Accordingly, the electron-phonon coupling (EPC) in 3LW/224L-hBN vdWHs happens between localized electrons confined within WS_2 constituents and bulk-like LB phonons involving all of the layers, named a cross-dimensional EPC. In addition, the specific frequency of LB phonons is well reproduced by extending LCM to include the interface force constant. The built-up cross-dimensional EPC in vdWHs allows new access to manipulate both the designable phonon excitations and the coupling to the localized electronic states by changing the constituents and interface engineering.

Surprisingly, the strong interaction between 2DM and its supported substrate behaviors is just like a spring to active the sample-substrate interface vibration modes, as shown in Fig. 3(d). The low-frequency Raman spectra of 1L-WS_2 samples as grown on both sapphire and silicon substrates clearly show an interface mode with its frequency close to $\sim$30 cm^{-1} (Xiang et al., 2021). The distinguish of its origin from those low-frequency interlayer S and LB modes is by noticing the monolayer feature of WS_2 sample. It is shown that the strong sample-substrate interface stems from the unavoidable interface tensile strain introduced in the process of CVD growth, which is not supposed to exist in 2DMs obtained by mechanical exfoliation. Statistically, the frequencies of interface vibration peaks are quite similar for various as-grown WS_2 flakes, ruling out the possible sample-dependent phonon behaviors. These results introduce low-frequency Raman spectroscopy as an effective tool in probing sample-substrate interactions which are naturally subject to 2DMs.

Surface vibration modes

Surface vibration modes, as the microscopic interface mode of an SL (Fig. 2(a)), specify those modes strongly localized near the surface. In the multilayer 2DMs, the interlayer vibrations introduced above hold a branch of surface modes, as illustrated in Fig. 4(a) by the dashed line for multilayer graphenes, where the atomic displacements become much more surface-confined as the number of layers increases (Tan et al., 2012). The corresponding frequency in the bulk case must be zero as expected from the descending trend of the branch. Another example of surface mode is the radial breathing mode (RBM) of a SWNT, which corresponds to the coherent vibration of the carbon atoms in the radial direction, as if the tube were "breathing" (Saito et al., 1998), as shown in Fig. 4(b). It can be constructed by the roll-up of an out-of-plane transverse acoustic phonon (oTA) at Γ point in

the BZ of monolayer graphene. RBM features are unique to carbon nanotubes and occur with frequencies between 120 and 350 cm^{-1} for SWNTs for diameters in the range 0.7 nm $< d_t <$ 2 nm (Dresselhaus et al., 2005), as shown in Fig. 4(b). The relation of RBM frequency (ω_{RBM}) on d_t is expressed by $\omega_{RBM} = A/d_t + B$ with A and B parameters determined experimentally. The reciprocal dependency of ω_{RBM} on d_t is a result of spatial confinements along the circumferential direction of the SWNT. RBM features find the applications to study d_t, to probe the electronic structure through its intensity (I_{RBM}) and to perform an (n, m) assignment of a single isolated SWNT from analysis of both d_t and I_{RBM}, as to be introduced in the section "Resonance Raman scattering in nanostructures."

In contrast to the long SWNT, there are both RBMs and confined extensional (EXT.) vibration modes vibrating along the long axis of the nanorod, (Miscuglio et al., 2016), as illustrated in Fig. 4(c). Different from SWNT, ω_{RBM} of a nanorod is described by

$$\omega_{RBM} = \frac{2\tau_n}{D}\sqrt{\frac{E(1-v)}{\rho(1+v)(1-2v)}} \tag{11}$$

with D the diameter of the nanorod, ρ the mass density, E the Young modulus, v the Poisson ratio, and τ_n the nth root of the equation $\tau J_0(\tau) = (1-2v)/(1-v)J_1(\tau)$. $J_0(\tau)$ and $J_1(\tau)$ are Bessel functions. The frequency of the confined EXT. mode is given by

$$\omega_{EXT} = \frac{2n+1}{L}\pi\sqrt{E_{||}/\rho} \tag{12}$$

where L is the nanorod length, $E_{||}$ is the Young modulus along the long axis of the nanorod. The factor (2n + 1) with $n = 0, 1, 2, \ldots$, accounts for the number of confined modes. The confined EXT. mode has a smaller frequency ($\sim$7.5 cm^{-1}) with respect to the RBM ($\sim$15.7 cm^{-1}) because of the fewer confinements in the long axis. To hybrid nanorod with a nanodot to form the dot-in-rods (like CdSe/CdS core-shell) structure is prominent for light-emitting applications (Bruchez et al., 1998). The dot-in-rods hybrid structure has interesting impacts on the confined surface vibrations (Miscuglio et al., 2016). Unlike nanorods, the fundamental acoustic vibrations of a nanodot are separated into ellipsoidal (ELL.) and spheroidal modes (RBMs), whose frequencies can be obtained by Lamb's theory and assigned by the radial (n) and angular quantum (l) numbers. Accordingly, $l = 0$ represents the spheroidal modes with their frequencies expressed by

$$\omega_{RBM,n} = S_n\frac{2c_L}{D} \tag{13}$$

where c_L is longitudinal sound velocity, D is the diameter of the sphere, and the first two coefficients for $n = 1, 2$ are $S_1 = 2.87$ and $S_2 = 6.16$. The Raman spectrum of a CdSe nanodot (D$\sim$5.7 nm) is shown in Fig. 4(c) with each mode explicitly assigned by a (n, l). Noted its $\omega_{RBM,\,0} \sim 16.5$ cm^{-1} is much close to that in CdS nanodot ($\omega_{RBM} \sim 15.7 cm^{-1}$). Fig. 4(c) shows the Raman spectrum of a CdSe/CdS dot-in-rods, with $D\sim$5.7 nm for CdSe dot and $D\sim$5.75 nm for CdS rod. The Raman peak of the confined EXT. mode is much similar to that of the nanorod. It can be attributed to the nonlocality of this vibration that extends over the full rod volume and therefore is less affected by the local modification of the core. However, the RBM peak is divided into a fundamental RBM (F-RBM) and a high-order RBM (H-RBM). As illustrated by the inset in Fig. 4(c), F-RBM shows a symmetric dilatation/contraction motion located in the central region of the rod, while H-RBM exhibits a symmetric oscillation off-center of the rod. The splitting of F-RBM and H-RBM increases with increasing core size. This can be understood in the way that dot-in-rods architecture leads to a reduction of the sound velocity in the core region of the rod. Dot-in-rods architecture can be exploited as a tool to tune exciton-phonon coupling in nanocrystal heterostructures.

Surface optical (SO) vibration modes were first predicted by Fuchs and Kliewer (1965) and first observed by Ibach using inelastic electron scattering (Ibach, 1970). The dispersion relation of a SO mode in an infinitely long cylindrical wire can be written (in the limit $q \gg \omega/c$)

$$\omega_{SO}^2 = \omega_{TO}^2 + \frac{\omega_p^2}{\varepsilon_\infty + \varepsilon_m f(x)} \tag{14}$$

with $x = qr$, where ω_{TO} is the TO mode frequency at zone center, ω_p is the screened ion plasma frequency given by $\omega_{LO}^2 = \omega_{TO}^2 + \omega_p^2/\varepsilon_\infty$, ε_∞ is the high-frequency dielectric constant of bulk materials, ε_m is the dielectric constant of the overlaying media to wire, $d = 2r$ is the wire diameter, and $f(x)$ is obtained from the eigenvalue equation

$$f(x) = \frac{I_0(x)K_1(x)}{I_1(x)K_0(x)} \tag{15}$$

with $I_j(x)$ and $K_j(x)$ are Bessel functions. Raman spectra of GaP nanowires in air ($\varepsilon_m = 1$), dichloromethane ($\varepsilon_m = 2$), and aniline ($\varepsilon_m = 2.65$) are plotted in Fig. 4(d) (Gupta et al., 2003). They feature two sharp peaks, which are identified with the TO ($q = 0$) and LO ($q = 0$) modes, in reasonable agreement with bulk crystalline GaP, and a third one assigned to SO by its sensitivity to the interfaced external medium. Noted, unlike the surface acoustic modes discussed above, the observation of SO mode here is enabled by an inherent length scale ($\sim$40 nm) in the nanowires due to either the self-oscillating nature of the filament cross section or polynuclear growth (Gupta et al., 2003).

Folded vibration modes

Folded vibrations modes in a binary SL stem from the new 1D out-of-plane translational periods of the alternating layers (Cardona and Guntherodt, 1989), i.e., $L = n_1a_1 + n_2a_2$, where $d_1 = n_1a_1$ and $d_2 = n_2a_2$ are layer thickness for AlAs and GaAs, as

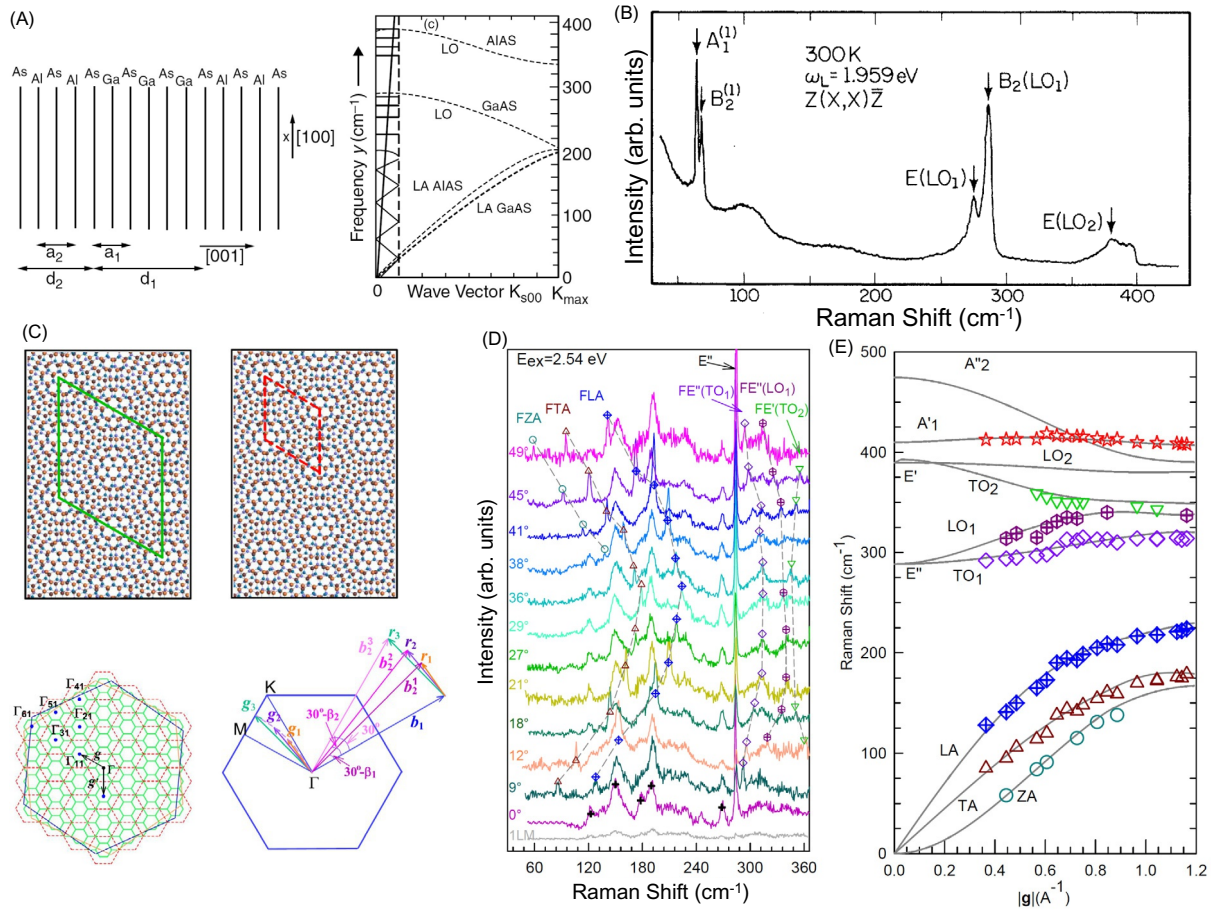

Fig. 5 (a) Sketch of GaAs/AlAs SL structure and dispersion curves of a photon (oblique solid line) and longitudinal phonons of bulk GaAs and AlAs (dashed line) and SL (solid line) (b) Raman spectrum of SL GaAs/AlAs. $A_1^{(1)}$ and $B_2^{(1)}$ are assigned to the folded acoustic phonons. (c) Top: Crystallographic SL and moiré pattern in (5,7)-tBLM with $\theta = 10.99^{\circ}$. Dashed (red) and solid (green) parallelogram corresponds to the moiré unit cell and crystallographic SL unit cell of the tBLMs, respectively. Bottom (left): the reciprocal lattice of (5,7)-tBLMs. The large blue and orange hexagons are the first BZ of top and bottom MoS_2 layers, and the dashed (red) and solid (green) hexagons represent the Wigner-Seitz cells of the reciprocal lattices corresponding to the moiré and crystallographic SL, respectively. Bottom (right): Schematic diagram of moiré basic vectors (g_i, $i = 1, 2, 3$) for $\theta \leq 30^{\circ}$. (d) Raman spectra of tBLMs in the region of 50–365 cm^{-1}. Different shapes and color symbols represent the Raman modes in different phonon branches. The Raman spectra of 1LM and 3R-BLM ($\theta = 0^{\circ}$) are plotted for comparison. (e) The comparison of calculated and experimental frequencies of moiré phonons dependent on $|\mathbf{g}|$. Panel (a): Reproduced from Zhang S.-L. (2012) *Raman Spectroscopy and its Application in Nanostructures*. John Wiley & Sons Ltd. Panel (b): Reproduced from Colvard et al. (1980) *Physical Review Letters* 45: 298–301. Panels (c–e): Reproduced from Lin et al. (2018) *ACS Nano* 12(8): 8770–8780.

shown in Fig. 5(a) for $n_1 = 3$ and $n_2 = 2$, respectively. The original BZ in bulk case, $-\pi/a$ to π/a, now is folded into a small one in SL, $-\pi/L$ to π/L. The folded optical phonons in AlAs and GaAs are strongly confined within each layer (confined vibration modes). But the acoustic phonons which are similar to each other in AlAs and GaAs produce ($p = n_1 + n_2$) folded phonons, as illustrated in Fig. 5 (a) for $p = 8$. Interestingly, the non-intersect optical and acoustic branches in bulk GaAs and AlAs now overlap with each other, which makes the acoustic phonon Raman active in the GaAs/AlAs SL. Fig. 5(b) shows the Raman spectrum of a GaAs/AlAs SL which presents a folded acoustic doublet ($A_1^{\{1\}}$ and $B_2^{\{1\}}$) (Colvard et al., 1980).

Instead of the 1D out-of-plane translational periods along the growth direction in the semiconductor SL, as drawn in Fig. 5(a), in-plane 2D translational periods are recently discovered in the twisted bilayer (tBL-) 2DMs (Cao et al., 2018), as firstly exampled by graphene and then rapidly extended to other 2DMs. It is achieved by rotating (with an angle θ) the two crystal networks in bilayer system with respect to each other. Fig. 5(c) shows the crystallographic and moiré SLs for tBL-MoS_2 with $(m, n) = (5,7)$, denoted as (5,7)-tBLM (Lin et al., 2018). The corresponding $\theta = 10.99^{\circ}$ is obtained based on the relation $\cos\theta = (m^2 + 4mn + n^2)/2(m^2 + mn + n^2)$. The lattice constants for crystallographic (L) and moiré (L^M) SLs are receptively, $L = a_0 \mid m - n \mid /2 \sin(\theta/2)$ and $L^M = a_0/2 \sin(\theta/2)$. They are equal for the case of $\mid m - n \mid = 1$. The Wigner-Seitz cells corresponding to crystallographic and moiré SLs are shown in Fig. 5(c), which clearly divide the first BZs of top and bottom monolayers into the small hexagons. The magnitude of the moiré reciprocal lattice vector ($\mathbf{g}$) is obtained by $|\mathbf{g}| = 2b \sin(\theta/2)$, with $b = 4\pi/\sqrt{3}a_0$. The trace of $\mathbf{g}$ in the first BZ of the monolayer MoS_2 (1LM) as a function of θ is demonstrated in Fig. 5(c). It indicates that the phonons of 1LM with $\mathbf{q} = \mathbf{g}$ are folded back to the Γ points in the Wigner-Seitz cells and accordingly become Raman active. The Raman spectra of tBLM with θ ranging from 0° to 49° are

shown in Fig. 5(d). Seven series of θ-dependent Raman modes are identified as folded vibration modes associated with ZA, TA, LA, E″(TO_1), E″(LO_1), E′(TO_2) and A_1′ branches in 1LM, accordingly assigned as FZA (F stands for "folded"), FTA, FLA, FE″(TO_1), FE″(LO_1), FE′ (TO_2) and FA_1′, respectively. Fig. 5(e) shows the experimental frequencies of moiré phonons mapped onto the theoretical dispersion curves traced by **g**. The good agreement indicates that the moiré phonons can serve as a fingerprint to determine θ of the tBLMs.

Similar to the confined folded optical phonons in each alternating quantum potential well, as shown in Fig. 2(a), the optical phonons of tBL-2DMs are confined within the in-plane moiré potential well. The strength of confinements becomes extremely strong as θ gets much close to zero, as exampled by the tBL-graphene (tBLG) with $\theta = 0.987^{\circ}$ (it corresponds to $L^M/a_0 \sim 3328$). It makes the G-band due to the stretching of the C—C bonds highly localized at those regions referred to as AB- and BA-stacked domains, strain solitons (SP) and topological points (AA) (Gadelha et al., 2021). To probe those G-bands, including G_r^+ from SP region and G_r^- from AA region, needs a nano-Raman spectroscope. These strongly confined moiré phonons are helpful to understand phonon-related effects at atomic and nanometric scales, such as Jahn-Teller effects (Angeli et al., 2019; Shinozuka, 2021) and electronic Cooper pairing (Lian et al., 2019; Wu et al., 2018b).

Resonance Raman scattering in nanostructures

RRS is key to detecting those Raman peaks subject to weak intensities in both bulk cases and nanostructures. But RRS in nanostructures may show distinctive or even anomalous features. As discussed in the section "Raman spectroscopy basics," Raman shift is not dependent on the exploited incident laser wavelength, which is considered as one general rule for Raman scattering effect. Fig. 6(a) shows the Raman spectra of monolayer graphene under different excitation energies, whose 2D-band (Note 2D is not referred as "two-dimensional," but double of D-band in frequency.) is linearly dispersive as E_L increases, with a slope of ~ 100 $cm^{-1}eV^{-1}$, in contrast to the G-band (Wu et al., 2018a). The microscopic intra-valley and inter-valley scattering

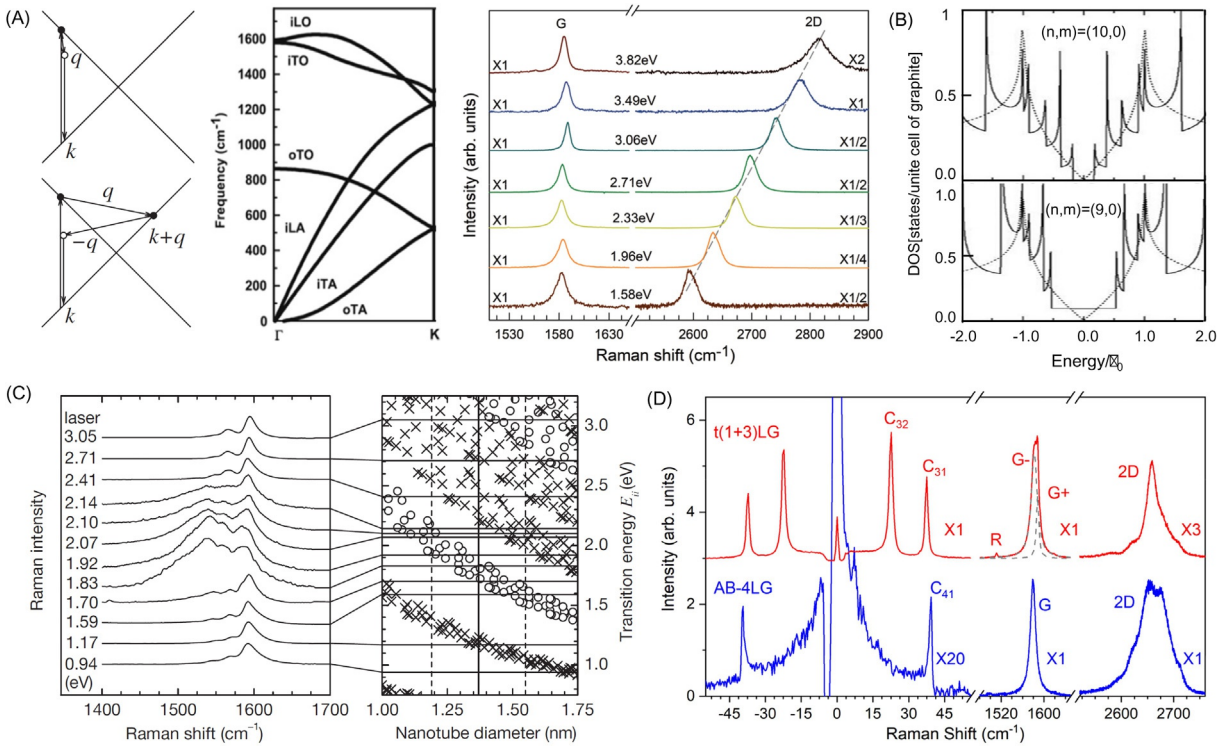

Fig. 6 (a) Left: One-phonon first-order and two-phonons second-order, resonance Raman spectral processes in monolayer graphene. Middle: Phonon dispersion of monolayer graphene. Right: Raman spectra of monolayer graphene measured at various excitations in the G- and 2D-bands regions. (b) The electronic 1D density of states (DOS) per unit cell for two (n,0) zigzag nanotubes: (up panel) the (9,0) nanotube which has metallic behavior, (bottom panel) the (10,0) nanotube which has semiconducting behavior. Also shown is the DOS for the graphene sheet. (c) Left: Raman spectra of the tangential G-band modes of SWNT bundles measured with several different laser lines, on a sample with $d_t = 1.37 \pm 0.18$ nm. Right: Resonant transition energies E_{ii} vs d_t. The vertical solid line is the average d_t and the vertical dashed lines denote the d_t distribution width. Crosses are for semiconducting SWNTs and open circles for metallic SWNTs. (d) Raman spectra of AB-stacked 4LG and t(1 + 3)LG in the regions of C, R-, G- and 2D-bands. C_{31} and C_{32} denote the observed shear modes in t(1 + 3) LG, which is from the 3LG constituent, in contrast to C_{41} in AB-stacked 4LG. The dashed lines are fit to G-band, which features two subpeaks, G^- and G^+, in t(1 + 3) LG. Panel (a): Reproduced from Wu et al. (2018) *Chemical Society Review* 47: 1822–1873. Panel (b): Reproduced from Saito et al. (1998) *Physical Properties of Carbon Nanotubes.* Imperial College Press. Panels (a (left and middle) and c): Reproduced from Jorio et al. (2011) *Raman Spectroscopy in Graphene Related Systems*, Weinheim: Wiley-VCH Verlag GmbH & Co. KGaA.

processes for G- and 2D-bands are shown in Fig. 6(a) (Jorio et al., 2011). G-band belongs to one-phonon (the degenerate TO/LO) first-order. scattering process with $q \sim 0$ (Γ point). 2D-band involves a two-phonon (two TO near K point) second-order scattering process, which has a $q \sim 2k \sim$ K (BZ boundary). $E_L = (E_m - E_i)$, proportional to k, applies to all the vertically electronic transitions, which is responsible for the strong Raman intensity observed in monolayer graphene which just has one atomic layer. On the other hand, ω_q of TO phonon is linearly increased as q gets away from the K point due to Kohn anomaly (Lazzeri and Mauri, 2006) (Fig. 6(a)). Accordingly, the increasing E_L (i.e., k) will lead to an increase in ω_q through the momentum conservation law $q \sim 2k$. Notably, q involved in the Stokes and anti-Stokes for the 2Dband are different from each other, creating a frequency discrepancy between its Stokes and anti-Stokes components (Cong et al., 2018; Tan et al., 1998) due to the dispersive feature of TO phonon (Thomsen and Reich, 2000). Such a frequency discrepancy had been widely detected in bulk graphite, graphite whiskers, and multi-walled carbon nanotubes.

The above discussion indicates the RRS in nanostructures is tightly associated with their electronic transitions which are mediated by the density of states (DOS). Of particular interest has been the 1D DOS in a carbon nanotube (Saito et al., 1998), as exampled by metallic (9,0) and semiconducting (10,0) zigzag nanotubes in Fig. 6(b). The DOS has a value of zero for the semiconducting nanotubes at $E = 0$ but is non-zero (and small) for the metallic nanotubes. The comparison between the 1D DOS for nanotubes and the 2D DOS for a graphene layer is included in Fig. 6(b). Nanotube exhibits lots of sharp peaks, which leads to the DOS-enhanced electronic transition as compared with graphene. A pair of sharp peaks in symmetry with respect to $E = 0$ specifies the resonance transition energy E_{ii}. Fig. 6(c) shows the Raman spectra of G-band modes of carbon nanotube bundles measured under different laser lines (Pimenta et al., 1998). The lineshapes indicate the presence of both semiconducting and metallic carbon nanotubes in bundles. Kataura plot was proposed to interpret the RRS effects in nanotubes, where Kataura and co-workers displayed the optical transition energies for each (n, m) SWNT as a function of tube diameter d_t (Kataura et al., 1999), as shown in Fig. 6(c). As demonstrated by the links between the Raman spectra and Kataura plot, RRS in bundles resonantly probes the SWNT with different d_t. Only those SWNTs with E_{ii} closed to the laser energy E_L are present in the Raman spectra. Alternatively, as indicated by the vertical lines in Fig. 6(c), G-band of a SWNT with a fixed d_t will not show up unless $E_L = E_{ii}$. In this way, RRS finds its valuable role to study the confined electronic structure in nanostructures.

The shear mode of multilayer graphenes is usually denoted as the C mode (Tan et al., 2012; Wu et al., 2014), which features a BWF line shape in AB-stacked multilayer graphene, as exampled by a four-layer graphene (AB-4LG) in Fig. 6(d). It is attributed to the quantum interference between the C mode and a continuum of electronic transitions near K point (Tan et al., 2012). As shown in Fig. 6(d), the intensity of C_{41} is much weak than G-band due to its small strength of electron-phonon coupling. However, the intensities of the S modes in a twisted (1 + 3) LG, labeled as t(1 + 3) LG, are comparable to the G-band. They are enhanced by the RRS processes mediated by the pairs of parallel electronic bands, induced by the intralayer twisting. This intensity enhancement of the S mode masks the weak BWF profile to give an overall Lorentzian profile, even though there is no band gap opening near K point in t(1 + 3) LG (Wu et al., 2014).

Conclusion

Raman spectroscopy has been used to study the science of nanostructures, recovering more and more fundamental aspects of their electronic and vibrational properties. In this encyclopedia, we firstly introduce the basics to understand the Raman scattering effect and the general features of a Raman spectrum. Followed is given to the phonon in nanostructures based on their Raman spectra, which is firstly exampled by a semiconductor SL and then extended to other cases. Of particular interest is RRS in nanostructures, which can be exploited to significantly enhance the weak Raman peaks and to probe the confined electronic structures. The rapid developments of Raman spectroscopy applied into nanostructures are readily beneficial from the non-stop improvements in experimental techniques, such as the nano-Raman spectroscope and the available laser lines for RRS. For the future perspectives, developing the specific Raman spectroscopy to allow the measurements of nanostructures under extreme environments, such as ultra-high pressure, ultra-strong magnetic field, extreme low-temperature, is desirable to find/address more and more fundamental questions, about electron-electron correlation, excitonic effects and electron-phonon interactions, etc., and the new physics in nanostructures.

Acknowledgment

We acknowledge support from the National Natural Science Foundation of China (Grant No. 11874350 and 12174381) and CAS Key Research Program of Frontier Sciences (Grant nos. ZDBS-LY-SLH004 and XDPB22).

References

Angeli M, Tosatti E, and Fabrizio M (2019) Valley Jahn-Teller effect in twisted bilayer graphene. *Physical Review X* 9: 041010.

Bottani CE, Mantini C, Milani P, Manfredini M, Stella A, Tognini P, Cheyssac P, and Kofman R (1996) Raman, optical-absorption, and transmission electron microscopy study of size effects in germanium quantum dots. *Applied Physics Letters* 69(16): 2409–2411.

Bruchez M, Moronne M, Gin P, Weiss S, and Alivisatos AP (1998) Semiconductor nanocrystals as fluorescent biological labels. *Science* 281(5385): 2013–2016.

Cao Y, Fatemi V, Fang S, Watanabe K, Taniguchi T, Kaxiras E, and Jarillo-Herrero P (2018) Unconventional superconductivity in magic-angle graphene superlattices. *Nature* 556(7699): 43–50.

Cardona M (1975) *Light Scattering in Solids*. Berlin Heidelberg: Springer-Verlag.

Cardona M and Guntherodt G (1989) *Light Scattering in Solids V: Superlattices and Other Microstructures*. Berlin Heidelberg: Springer-Verlag.

Colvard C, Merlin R, Klein MV, and Gossard AC (1980) Observation of folded acoustic phonons in a semiconductor superlattice. *Physical Review Letters* 45: 298–301.

Comas F, Trallero-Giner C, and Cantarero A (1993) Optical phonons and electron-phonon interaction in quantum wires. *Physical Review B* 47: 7602–7605.

Cong X, Wu JB, Lin ML, Liu XL, Shi W, Venezuela P, and Tan PH (2018) Stokes and anti-Stokes Raman scattering in mono- and bilayer graphene. *Nanoscale* 10: 16138–16144. https://doi.org/10.1039/C8NR04554B.

Davies JH (1997) *The Physics of Low-dimensional Semiconductors: An Introduction*. Cambridge University Press.

Demtroder W (2003) *Laser Spectroscopy: Basic Concepts and Instrumentation*, 3rd edn. Berlin Heidelberg: Springer-Verlag.

Dresselhaus M, Dresselhaus G, Saito R, and Jorio A (2005) Raman spectroscopy of carbon nanotubes. *Physics Reports* 409(2): 47–99.

Feng ZC, Mascarenhas AJ, Choyke WJ, and Powell JA (1988) Raman scattering studies of chemical-vapor-deposited cubic SiC films of (100) Si. *Journal of Applied Physics* 64(6): 3176–3186.

Fox M (2010) *Optical Properties of Solids*, 2nd edn. Oxford University Press.

Fuchs R and Kliewer KL (1965) Optical modes of vibration in an ionic crystal slab. *Physics Review* 140: A2076–A2088.

Gadelha AC, Ohlberg DAA, Rabelo C, Neto EGS, Vasconcelos TL, Campos JL, Lemos JS, Ornelas V, Miranda D, Nadas R, Santana FC, Watanabe K, Taniguchi T, van Troeye B, Lamparski M, Meunier V, Nguyen V-H, Paszko D, Charlier J-C, Campos LC, Cançado LG, Medeiros-Ribeiro G, and Jorio A (2021) Localization of lattice dynamics in low-angle twisted bilayer graphene. *Nature* 590(7846): 405–409.

Gupta R, Xiong Q, Mahan GD, and Eklund PC (2003) Surface optical phonons in gallium phosphide nanowires. *Nano Letters* 3(12): 1745–1750.

Ibach H (1970) Optical surface phonons in zinc oxide detected by slow-electron spectroscopy. *Physical Review Letters* 24: 1416–1418.

Jorio A and Saito R (2021) Raman spectroscopy for carbon nanotube applications. *Journal of Applied Physics* 129(2), 021102.

Jorio A, Saito R, Dresselhaus G, and Dresselhaus MS (2011) *Raman Spectroscopy in Graphene Related Systems*. Weinheim: WILEY-VCH Verlag GmbH & Co. KGaA.

Jusserand B, Paquet D, and Regreny A (1984) "Folded" optical phonons in $GaAs/Ga_{1-x}Al_xAs$ superlattices. *Physical Review B* 30: 6245–6247.

Kataura H, Kumazawa Y, Maniwa Y, Umezu I, Suzuki S, Ohtsuka Y, and Achiba Y (1999) Optical properties of single-wall carbon nanotubes. *Synthetic Metals* 103(1): 2555–2558. International Conference on Science and Technology of Synthetic Metals.

Lazzeri M and Mauri F (2006) Nonadiabatic kohn anomaly in a doped graphene monolayer. *Physical Review Letters* 97: 266407.

Lian B, Wang Z, and Bernevig BA (2019) Twisted bilayer graphene: A phonon-driven superconductor. *Physical Review Letters* 122: 257002.

Lin M-L, Tan Q-H, Wu J-B, Chen X-S, Wang J-H, Pan Y-H, Zhang X, Cong X, Zhang J, Ji W, Hu P-A, Liu K-H, and Tan P-H (2018) Moiré phonons in twisted bilayer MoS_2. *ACS Nano* 12(8): 8770–8780.

Lin M-L, Zhou Y, Wu J-B, Cong X, Liu X-L, Zhang J, Li H, Yao W, and Tan P-H (2019) Cross-dimensional electron-phonon coupling in van der Waals heterostructures. *Nature Communications* 10(1): 2419.

Miscuglio M, Lin M-L, Di Stasio F, Tan P-H, and Krahne R (2016) Confined acoustic phonons in colloidal nanorod heterostructures investigated by nonresonant raman spectroscopy and finite elements simulations. *Nano Letters* 16(12): 7664–7670.

Pimenta MA, Marucci A, Empedocles SA, Bawendi MG, Hanlon EB, Rao AM, Eklund PC, Smalley RE, Dresselhaus G, and Dresselhaus MS (1998) Raman modes of metallic carbon nanotubes. *Physical Review B* 58: R16016–R16019.

Piscanec S, Cantoro M, Ferrari AC, Zapien JA, Lifshitz Y, Lee ST, Hofmann S, and Robertson J (2003) Raman spectroscopy of silicon nanowires. *Physical Review B* 68: 241312.

Raman CV and Krishnan KS (1928) A new type of secondary radiation. *Nature* 121(3048): 501–502.

Richter H, Wang Z, and Ley L (1981) The one phonon Raman spectrum in microcrystalline silicon. *Solid State Communications* 39(5): 625–629.

Rücker H, Molinari E, and Lugli P (1992) Microscopic calculation of the electron-phonon interaction in quantum wells. *Physical Review B* 45: 6747–6756.

Saito R, Dresselhaus G, and Dresselhaus MS (1998) *Physical Properties of Carbon Nanotubes*. Imperial College Press.

Schuller C (2006) *Inelastic Light Scattering of Semiconductor Nanostructures: Fundamentals and Recent Advances*. Berlin Heidelberg: Springer-Verlag.

Shi W, Lin M-L, Tan Q-H, Qiao X-F, Zhang J, and Tan P-H (2016) Raman and photoluminescence spectra of two-dimensional nanocrystallites of monolayer WS_2 and WSe_2. *2D Materials* 3(2): 025016.

Shinozuka Y (2021) *Electron-Lattice Interactions in Semiconductors*, 1st edn. Jenny Stanford Publishing.

Smekal A (1923) Zur quantentheorie der dispersion. *Naturwissenschaften* 11: 873.

Smith E and Dent G (2019) *Modern Raman Spectroscopy: A Practical Approach*, 2nd edn. John Wiley & Sons Ltd.

Stroscio MA and Dutta M (2001) *Phonons in Nanostructures*. Cambridge University Press.

Sui Z, Leong PP, Herman IP, Higashi GS, and Temkin H (1992) Raman analysis of light-emitting porous silicon. *Applied Physics Letters* 60(17): 2086–2088.

Tan P-H (2019) *Raman Spectroscopy of Two-Dimensional Materials*. Springer International Publishing AG.

Tan PH, Bougeard D, Abstreiter G, and Brunner K (2004) Raman scattering of folded acoustic phonons in self-assembled Si/Ge dot superlattices. *Applied Physics Letters* 84: 2632–2634. https://doi.org/10.1063/1.1691171.

Tan PH, Deng YM, and Zhao Q (1998) Temperature-dependent Raman spectra and anomalous Raman phenomenon of highly oriented pyrolytic graphite. *Physical Review B* 58: 5435–5439. https://doi.org/10.1103/PhysRevB.58.5435.

Tan PH, Han WP, Zhao WJ, Wu ZH, Chang K, Wang H, Wang YF, Bonini N, Marzari N, Pugno N, Savini G, Lombardo A, and Ferrari AC (2012) The shear mode of multilayer graphene. *Nature Materials* 11(4): 294–300.

Thomsen C and Reich S (2000) Double resonant Raman scattering in graphite. *Physical Review Letters* 85: 5214–5217. https://doi.org/10.1103/physrevlett.85.5214.

Toporski J, Dieing T, and Hollricher O (2018) *Confocal Raman Microscopy*, 2nd edn. Springer International Publishing AG.

Wu J-B, Zhang X, Ijäs M, Han W-P, Qiao X-F, Li X-L, Jiang D-S, Ferrari AC, and Tan P-H (2014) Resonant Raman spectroscopy of twisted multilayer graphene. *Nature Communications* 5(1): 5309.

Wu J-B, Lin M-L, Cong X, Liu H-N, and Tan P-H (2018a) Raman spectroscopy of graphene-based materials and its applications in related devices. *Chemical Society Reviews* 47: 1822–1873.

Wu F, MacDonald AH, and Martin I (2018b) Theory of phonon-mediated superconductivity in twisted bilayer graphene. *Physical Review Letters* 121: 257001.

Xiang Q, Yue X, Wang Y, Du B, Chen J, Zhang S, Li G, Cong C, Yu T, Li Q, and Jin Y (2021) Unveiling the origin of anomalous low-frequency Raman mode in CVD-grown monolayerWS_2. *Nano Research* 14(11): 4314–4320.

Yoshikawa M, Mori Y, Obata H, Maegawa M, Katagiri G, Ishida H, and Ishitani A (1995) Raman scattering from nanometer-sized diamond. *Applied Physics Letters* 67(5): 694–696.

Yu PY and Cardona M (2010) *Fundamentals of Semiconductors: Physics and Materials Properties*, 4th edn. Berlin Heidelberg: Springer-Verlag.

Zhang S-L (2012) *Raman Spectroscopy and its Application in Nanostructures*. John Wiley & Sons Ltd.

Zhang X, Han WP, Wu JB, Milana S, Lu Y, Li QQ, Ferrari AC, and Tan PH (2013) Raman spectroscopy of shear and layer breathing modes in multilayerMoS_2. *Physical Review B* 87: 115413.

Zhang X, Qiao X-F, Shi W, Wu J-B, Jiang D-S, and Tan P-H (2015) Phonon and raman scattering of two-dimensional transition metal dichalcogenides from monolayer, multilayer to bulk material. *Chemical Society Reviews* 44: 2757–2785.

Zhang X, Tan Q-H, Wu J-B, Shi W, and Tan P-H (2016) Review on the raman spectroscopy of different types of layered materials. *Nanoscale* 8: 6435–6450.

Zi J, Buscher H, Falter C, Ludwig W, Zhang K, and Xie X (1996) Raman shifts in Si nanocrystals. *Applied Physics Letters* 69(2): 200–202.